JOURNAL OF CATALYSIS **170,** 311–324 (1997)
ARTICLE NO. CA971782

Nickel-Catalyzed Conversion of Activated Carbon Extrudates into High Surface Area Silicon Carbide by Reactive Chemical Vapour Deposition

R. Moene,[1] F. W. Tazelaar, M. Makkee,[2] and J. A. Moulijn

Department of Chemical Engineering, Section Industrial Catalysis, Delft University of Technology, Julianalaan 136, 2628 BL Delft, The Netherlands

Received January 2, 1997; revised May 20, 1997; accepted May 30, 1997

A novel method for the synthesis of high surface area silicon carbide extrudates has been developed which consists of applying nickel onto activated carbon extrudates followed by reaction with silicon tetrachloride and hydrogen. Utilization of nickel is shown to be essential in order to obtain a considerable conversion. Selective SiC formation has been obtained at 1380 K and 10 kPa. Thus, methane is formed at the interior of the carbon *via* gasification: $C(s) + 2H_2(g) \rightleftarrows CH_4(g)$, which subsequently reacts with silicon tetrachloride to silicon carbide: $SiCl_4(g) + CH_4(g) \rightleftarrows SiC(s) + 4HCl(g)$. The total carbon conversion ranges from 20 to 55% for nickel contents of 2 and 8 wt%, respectively. Si-codeposition will occur when the gasification reaction diminishes in time, due to deactivation of the nickel gasification sites. Extensive whisker formation of SiC is encountered owing to the operative vapour–liquid–solid mechanism. Mass transport calculations show that methane is formed throughout the extrudate, whereas the front of SiC formation moves from the outside to the internal part due to diffusion limitations of $SiCl_4$ and nickel deactivation. The residual carbon can be removed after conversion by oxidation, resulting in high surface area SiC extrudates. The BET-surface areas after conversion vary from 359 to 154 m^2/g; BET-surface areas after removal of the residual carbon are in the range of 57 to 32 m^2/g. Pore size distributions of the SiC supports show that the pore volume is evenly distributed over the meso- and macro-pore region (diameter: 2 to 100 nm) which allows the following areas of application: (1) reactions at high temperatures and (2) liquid-phase reactions at demanding pH conditions.

1. INTRODUCTION

Catalysts based on activated carbon hold several advantages over silica and alumina based catalysts. Reaction between the support and the active material is limited to a large extent to the inertness of the graphitic surface. This can result in many cases in an optimal utilization of the metals applied. An example is the hydrodesulfurization of thiophene by supported cobalt molybdenum catalysts. Catalysts based on activated carbon display a higher activity per unit weight metal compared to Co–Mo/Al_2O_3 catalysts (1). The same behaviour is found for Cu–Cr catalysts used in exhaust catalysis; i.e., high activities for the oxidation of CO and the reduction of NO have been reported for carbon based Cu–Cr catalysts (2). The thermostability of activated carbon in inert environments at elevated temperatures is considerably higher than that of SiO_2 and Al_2O_3; up to 1700 K no significant sintering of the support is observed. Another benefit of activated carbon is its stability in caustic and acidic solutions. The use of activated carbon as catalyst support is limited despite these beneficial properties due to its reactivity in oxidizing environments and poor mechanical strength. Catalysts based on activated carbon are, therefore, predominantly applied in liquid-phase reactions at demanding pH conditions, in which the advantages (applicability at demanding pH conditions) prevail over the disadvantages (considerable attrition at high stirring rates). For a review article on these advantages the authors like to refer to Jungten (3). The mechanical strength of activated carbon can be improved by employing special types of manufacturing methods or by modifying activated carbon by deposition of silicon carbide (SiC) (4), a very hard and oxidation resistant material. Significant improvements in mechanical strength and the resistance against oxidation can be achieved by chemical vapour deposition of SiC as well (5, 6). Synthesis of high surface area SiC, however, can render additional improvements that exceed those obtained by the surface modification of activated carbon. The last two decades much effort has been devoted to the development of high surface area nonoxidic ceramics (7–9). It comprises mainly carbides, nitrides, and borides of transition metals, which possess interesting properties regarding their catalytic activity and stability. Research for the development of nonoxidic catalyst supports has mainly been focused on the preparation of high surface area (i.e., larger

[1] Present address: Shell Research and Technology Centre, Amsterdam, Badhuisweg 3, 1031 CM Amsterdam, The Netherlands.
[2] Corresponding author. Fax: +31 15 2784452. E-mail: m.makkee@stm.tudelft.nl.

0021-9517/97 $25.00

than 20 m^2/g (10)) silicon carbide. The bulk properties of this material (an inert surface, high resistance against oxidation, and high mechanical strength) are claimed to provide a catalyst support with exceptional performance. Pham-Huu *et al*. (11) claimed for example for the isomerization of alkanes with MoO_3 on SiC no additional acidic sites, this in contrast to MoO_3 on alumina. Shaping of high surface SiC powder is expected to be laborious due to the low sinterability of the material. Utilization of a preformed precursor which exhibits good textural properties might resolve this obstacle. Conversion of activated carbon into SiC has potential in achieving high surface area SiC. Ledoux *et al*. (12) describe a method in which gaseous silicon monoxide (SiO) is reacted with activated carbon at 1400 K. Vannice *et al*. (13) describe the conversion of graphite powder into SiC by reacting it with $SiCl_4$ at temperatures exceeding 1600 K. The combination of the advantageous aspects of both procedures might lead to a process, in which $SiCl_4$ is utilized at low temperatures. The stability of activated carbon in a hydrogen environment, however, limits its reactivity to SiC formation below 1600 K (5). The application of catalysis for increasing the reactivity of the activated carbon may be the key for combining low temperature conversion with easily accessible reactants. In this article the influence of nickel on the conversion of activated carbon into high surface area SiC will be demonstrated. Both the chemical aspects regarding the carbon activation and SiC formation as well as the possible occurrence of mass-transfer limitations will be discussed.

2. EXPERIMENTAL

2.1. Materials

Activated carbon extrudates RW08, a peat based, steam activated carbon has been supplied by Norit. To assure the application of well-defined activated carbon, classification of the activated carbon extrudates of different degrees of activation has been carried out by fluidization of the extrudates in water for 2 h. After settling the content of the column was separated in five layers of which the degree of activation increased from bottom to top. The middle fraction has been used and will be referred to as RW08. The properties of this fraction are shown in Table 1. $Ni(NO_3)_2 \cdot 6H_2O$ (>99%) and silicon tetrachloride (>98%) were obtained from Janssen Chemica. The activated carbon extrudates (RW08) have been loaded with nickel by pore volume impregnation with a solution of $Ni(NO_3)_2$ in demineralized water to arrive at nickel contents of 2, 5, or 8 wt%. Drying was performed at atmospheric pressure in air at 385 K. The gases were purified by passing them over a Cu/Al_2O_3 (argon) or Pd/Al_2O_3 (hydrogen) catalyst, followed by drying by molecular sieve 5A.

TABLE 1

The Physical Properties of the Activated Carbon Extrudates

S_{BET} (m^2/g)	V_{pore} (ml/g)	S_t (m^2/g)	V_{micro} (ml/g)	ρ(Hg) (kg/m^3)	ρ(He) (kg/m^3)	Ash (%)	Length (mm)	Diameter (mm)
947	1.05	112	0.41	661	2167	5.2	3.0	0.81

2.2. Conversion of Activated Carbon Extrudates

A schematic picture of the CVD apparatus is shown in Fig. 1. A thin bed (length 1 mm) of dried extrudates (0.2 gram) is placed between two quartz wool pads in a tubular quartz reactor (ID 42 mm). The reactor is heated (0.167 K/s) under flowing hydrogen (0.18 mol/h) at 100 kPa to 1400 K and maintained at this temperature for 300 s. The reactor was subsequently cooled down to the desired reaction temperature. This procedure will be referred to as the pretreatment. The concomitant weight decrease for the 2, 5, and 8 wt% Ni/C systems was identical and amounted to 18%. The hydrogen flow was then increased to 3.69 mol/h followed by pressure adjustment of the reactor to 8 kPa. Gaseous silicon tetrachloride ($SiCl_4$) or methyl trichlorosilane (MTS, CH_3SiCl_3) were introduced using argon as carrier gas, while the pressure of the saturator was kept constant at 100 kPa. The flow rates of $SiCl_4$ and CH_3SiCl_3 were determined using their Antoine equations (14, 15) and amounted to 0.14 mol/h and 0.18 mol/h, respectively. After reaction the reactor was pressurized to 100 kPa and cooled down under flowing hydrogen to room temperature.

2.3. Removal of Residual Carbon

The residual carbon, present after conversion, has been removed by oxidation for 2 h in dry air at 1023 K in a tubular reactor.

2.4. X-Ray Diffraction (XRD)

X-Ray diffractograms of the extrudates were measured with a Philips powder diffractometer (PW1840) using Cu$K\alpha$ radiation (wavelength 0.154 nm).

2.5. Scanning Electron Microscopy (SEM)

A JEOL (JSM-35) scanning electron microscope has been used to determine the morphology of the deposited phases. An acceleration current of 15 to 20 keV has been applied; the samples have been sputtered with gold or platinum to suppress charging during SEM analysis.

2.6. Thermal Gravimetric Analysis (TGA)

TGA has been carried out on a Stanton Redcraft (STA-1500) thermobalance. Samples (20 mg) were oxidized in air using a temperature increase of 0.167 K/s from room

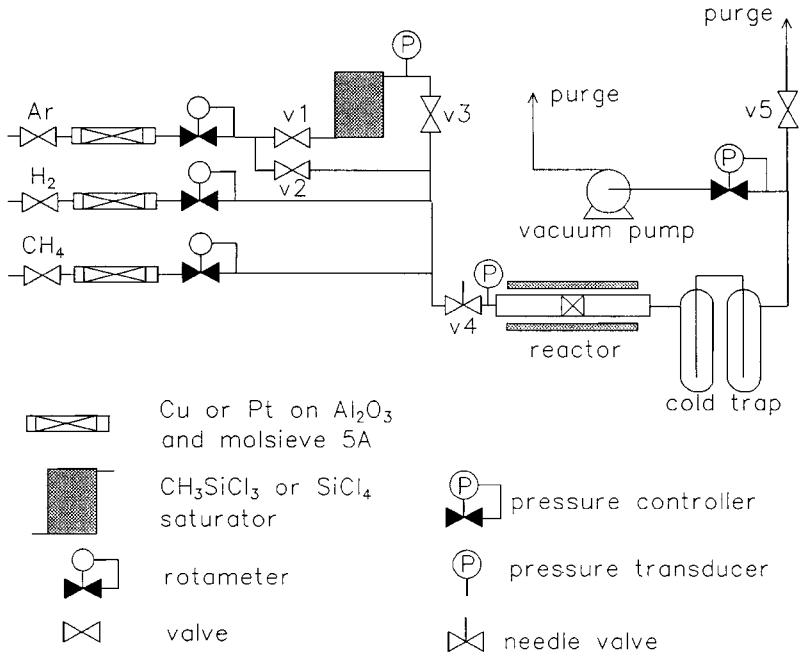

FIG. 1. Scheme of the CVD apparatus.

temperature to 1273 K. The weight change and concomitant heat flux were recorded simultaneously.

2.7. Surface Area Measurements

Nitrogen isotherms at 77 K were recorded on a Carlo Erba Sorptomatic 1800 after degassing at 423 K and 0.1 kPa. The BET surface area, pore volume, *t* surface area, and micro-pore volume were determined according to literature (16, 17).

3. RESULTS

3.1. Pretreatment

The applied nickel nitrate decomposes during the pretreatment into NiO and NO_x. XRD profiles of the pretreated extrudates show that NiO is subsequently reduced to metallic Ni by hydrogen.

3.2. Nickel Catalysis in the SiC Formation Utilizing $SiCl_4$

The influence of temperature on the nickel catalyzed SiC formation has been determined by XRD. Activated carbon extrudates loaded with 2 wt% Ni and reacted with $H_2/SiCl_4$ at 1075, 1250, and 1378 K have been analyzed. The results are visualized in Fig. 2. The XRD profile after reaction of $SiCl_4$ and H_2 with activated carbon in the absence of nickel at 1380 K is incorporated as a reference (curve a). No bulk SiC deposition is observed in this case. It can be concluded from curves b, c, and d, that the presence of nickel at temperatures above 1250 K favours SiC formation. Silicon co-deposition, however, still appears in this system at all temperatures investigated. The SiC morphology has been analyzed by SEM as shown by Figs. 3 to 6. Figure 3 displays the presence of SiC whiskers at the interior of the extrudate on which secondary nucleation developed. A SiC layer of 5 μm can be distinguished at the surface of the extrudate which consists of a cluster of SiC platelets as shown by Fig. 4. Bamboo-like SiC structures appear concomitantly (Fig. 5) of which the diameter equals that of the whiskers that are covered with platelets. Excessive whisker growth is encountered at the outside of the extrudate as

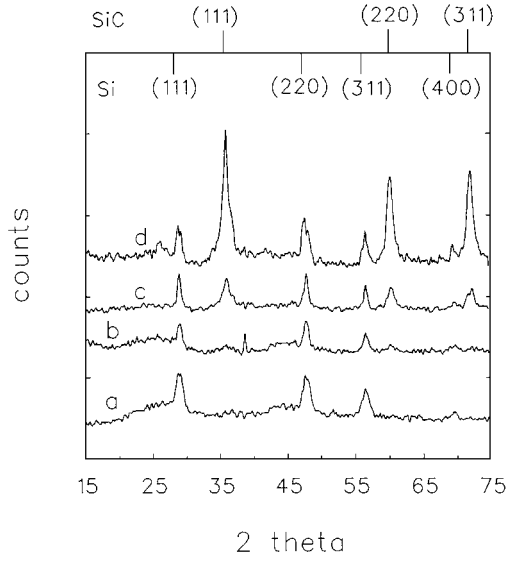

FIG. 2. XRD profiles of converted activated carbon, (a) without Ni-catalysis at 1380 K; (b), (c), and (d) 2 wt% Ni, 3600 s reaction, at 1075, 1250, and 1378 K, respectively.

FIG. 3. 10 μm. Secondary SiC growth on a SiC whisker $H_2/SiCl_4 = 26$; *T*, 1250 K; *P*, 8 kPa; *t*, 3600 s.

well (Fig. 6). Insight in the origin of codeposition of silicon after conversion at 1378 K can be achieved by XRD analysis of conversions at similar conditions with, however, a different time span of conversion and increased amounts of nickel applied. The results are displayed in Fig. 7. Selective SiC formation has been achieved after 600 s reaction for 2 wt% Ni and after 3600 s reaction, employing 5 wt% or 8 wt% Ni, respectively. SiC deposition is encountered as well on the quartz-wool pads downstream of the extrudates when 5 or 8 wt% Ni had been applied. A prolonged conversion time for the 5 wt% nickel loaded carbon results in Si codeposition, similar to the situation in which a conversion time of one hour and 2 wt% Ni has been applied. A stage, which precedes SiC growth, is apparent after 600 s utilizing 8 wt% nickel as shown by two broad peaks around values of 2θ of 25 and 45, which originate from the activated carbon. The absence of detectable crystalline nickel is remarkable, because XRD detects in all cases nickel after the pretreatment of the nickel loaded carbon. The following two processes, or a combination thereof, can account for this. Nickel either reacts with silicon tetrachloride in the initial stage to form an amorphous mixture Ni_xSi_y or redisperses into very small nickel crystallites owing to the high temperature applied. This initial period shifts subsequently towards SiC formation (curve f). Micrographs of extrudates converted at 1380 K show the abundance of homogeneously distributed whisker growth throughout the extrudate (1 to 2 μm in length, 0.15 μm in thickness) after SiC formation. Small SiC granules (0.1 μm diameter) can be distinguished as well. The presence of these two SiC-morphologies points to the existence of two types of mechanisms operative in the SiC formation.

The influence of methane on the conversion is depicted in Fig. 8. Silicon carbide formation is achieved at 1380 K in the absence of nickel (curve 8^c). The use of methane in the absence and presence of nickel has resulted in a minor codeposition of silicon as shown by diffractogram 8^b and 8^c, respectively. Peak broadening in curve 8^b implies the presence of a SiC structure with a higher stacking-fault density than that grown in the absence of additional CH_4. Micrographs of the SiC structure formed from a $SiCl_4/CH_4$ mixture in the presence of nickel are shown in Figs. 9 and 10. Extensive whisker growth is observed at the exterior of the extrudates. The whiskers are longer and thicker (0.2 to

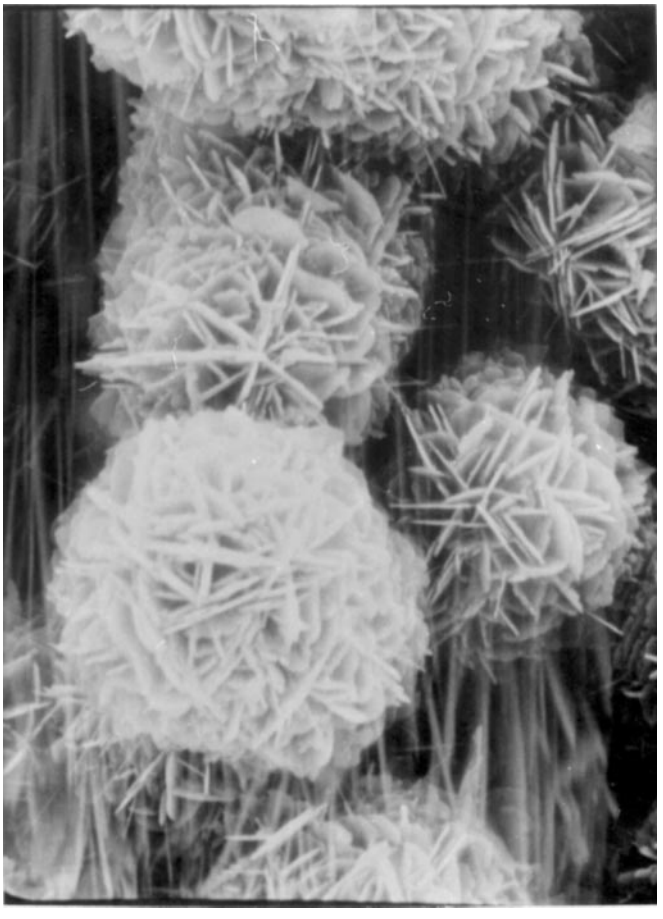

FIG. 4. 5 μm. A cluster of SiC platelets, $H_2/SiCl_4 = 26$; *T*, 1250 K; *P*, 8 kPa; *t*, 3600 s.

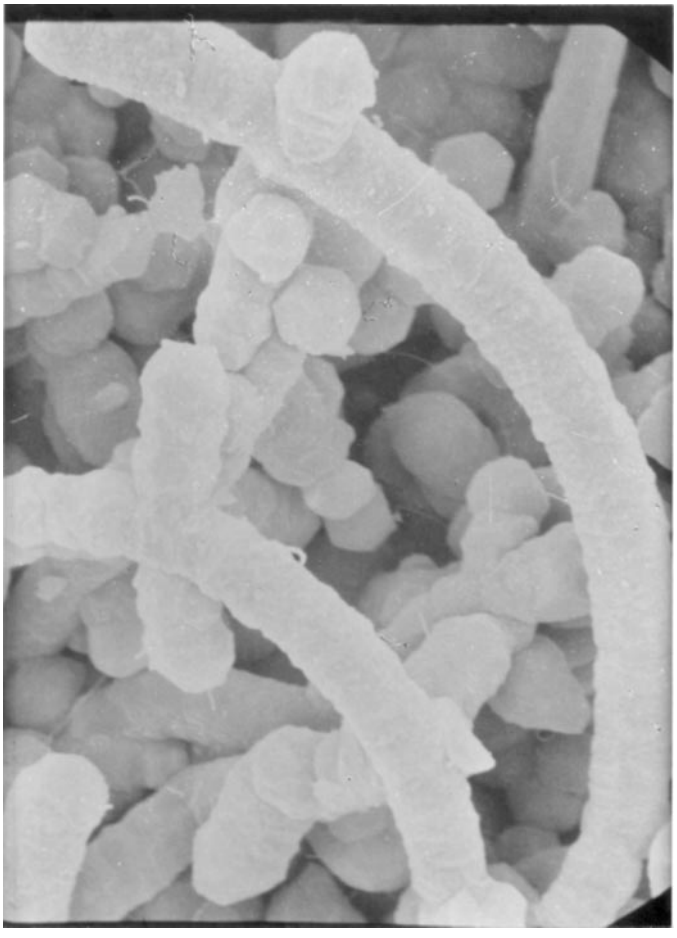

FIG. 5. 10 μm. Bamboo-like SiC structures formed by densification of a cluster of platelets, $H_2/SiCl_4 = 26$; *T*, 1250 K; *P*, 8 kPa; *t*, 3600 s.

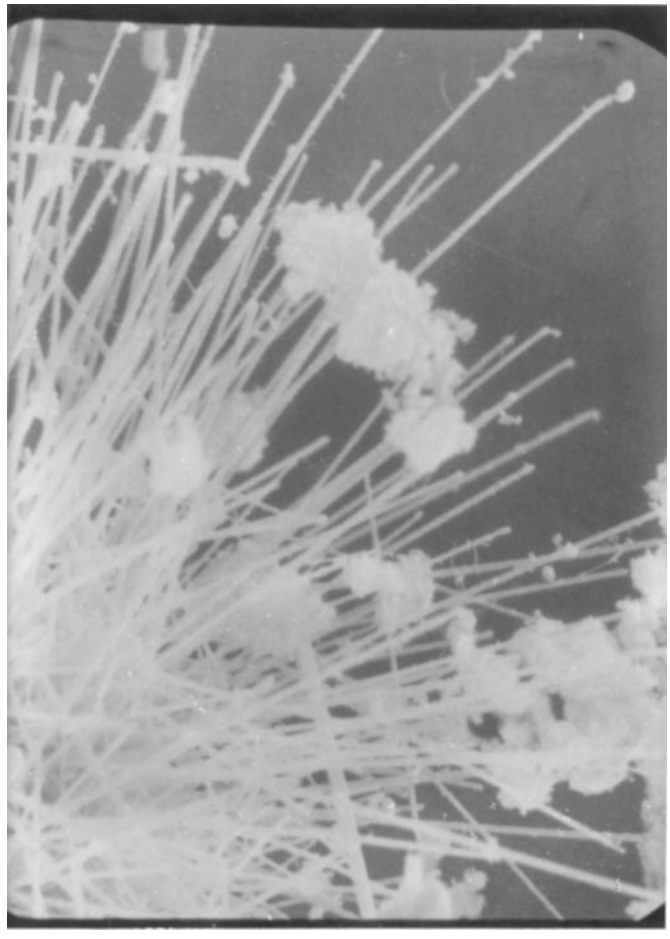

FIG. 6. 15 μm. Excessive whisker growth at the exterior of an extrudate, $H_2/SiCl_4 = 26$; *T*, 1380 K; *P*, 8 kPa; *t*, 3600 s.

0.5 μm) compared to those obtained in the absence of additional methane. The interior of the extrudate is densified to a large extent; SEM-analyses of several extrudates suggest the presence of a density gradient moving from the outside to the less denser inside.

Conversion of the carbon extrudates into SiC results in a weight increase owing to the deposition of silicon. Measuring this weight increase in combination with the amount free carbon present in the system permits the determination of a carbon and silicon mass balance. Table 2 displays the conversion conditions and corresponding weight increase. The second last column (Δw conv.) represents the weight increase after conversion of the carbon corrected for the weight loss during the pretreatment. The last column (*w* depos.) embodies the residual mass after oxidation of the nonconverted carbon amended for the ash content of the carbon including the applied nickel. This represents thus the amount of deposited silicon carbide and silicon. It is shown that moving from reaction temperatures of 1075 K to 1378 K causes an increase in the quantity of deposition when 2 wt% Ni has been employed. An additional enlargement is achieved at higher nickel amounts and longer deposition periods. The weight increase after one hour conversion is largest at the investigated reaction conditions when 5 wt% nickel has been applied. The residual mass after oxidation

TABLE 2

Characteristics of Conversion of Activated Carbon Extrudates, $H_2/SiCl_4 = 26$, $P = 8$ kPa

Exp. nr.	Ni cont. (wt%)	*T* (K)	*t* (s)	Δw conv.[a] (%)	*w* depos.[b] (%)
1	2	1075	3600	23.3	25.9
2	2	1250	3600	42.5	33.3
3	2	1378	3600	57.6	42.8
4	2	1376	600	31.7	29.0
5	5	1383	3600	67.8	54.4
6	5	1379	7200	75.2	55.9
7	8	1373	600	20.8	39.6
8	8	1379	3600	55.5	54.8
9[c]	5	1379	3600	82.5	44.8

[a] Δw conv. $= (w_t/(w_0 - w_{gasif.})^*100\%$.
[b] *w* depos. $= (w_{SiC} + w_{Si} - w_{ash})/(w_{SiC} + w_{Si} + w_{ash} + w_C)^*100\%$.
[c] Methane added ($CH_4/SiCl_4 = 2$).

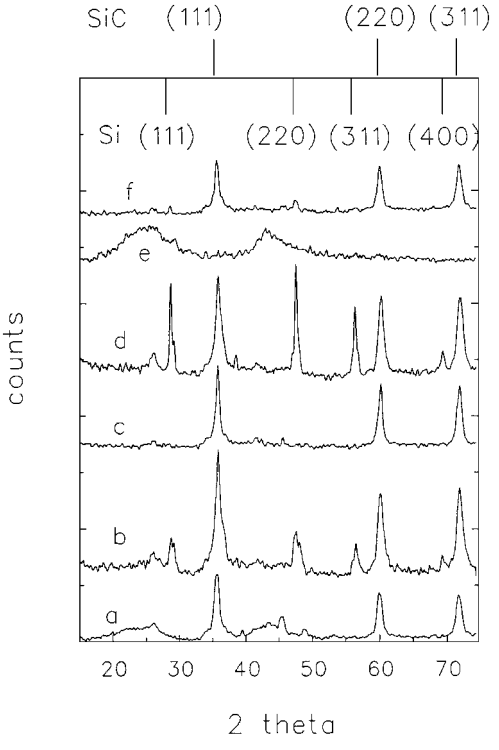

FIG. 7. XRD profiles of converted activated carbon 1378 K: (a) 2 wt% Ni, 600 s; (b) 2 wt% Ni, 3600 s; (c) 5 wt% Ni, 3600 s; (d) 5 wt% Ni, 7200 s; (e) 8 wt% Ni, 600 s; (f) 8 wt% Ni, 3600 s.

is, however, identical to that when 8 wt% Ni has been applied, after 3600 s deposition time.

3.3. *Catalyst Properties*

The extrudates converted at 1250 and 1380 K remain intact after removal of the nonconverted carbon by oxidation. The shape memory concept can thus be applied by using preshaped carbon bodies in order to synthesize shaped SiC.

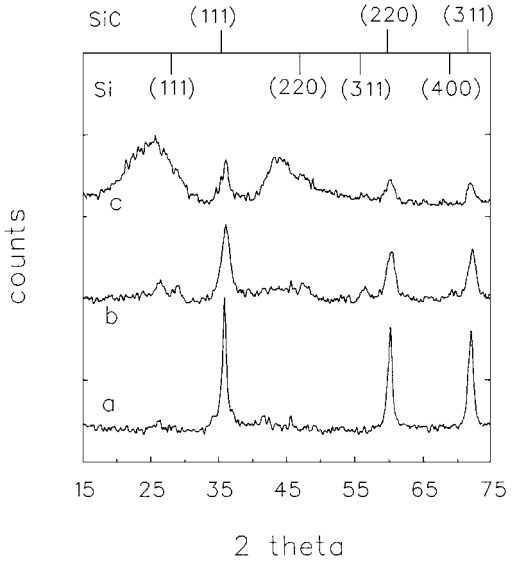

FIG. 8. XRD profiles, $H_2/SiCl_4 = 26$, reaction time 3600 s, 1380 K: (a) 5 wt% Ni; (b) 5 wt% Ni, $CH_4/SiCl_4 = 2$; (c) no nickel, $CH_4/SiCl_4 = 2$.

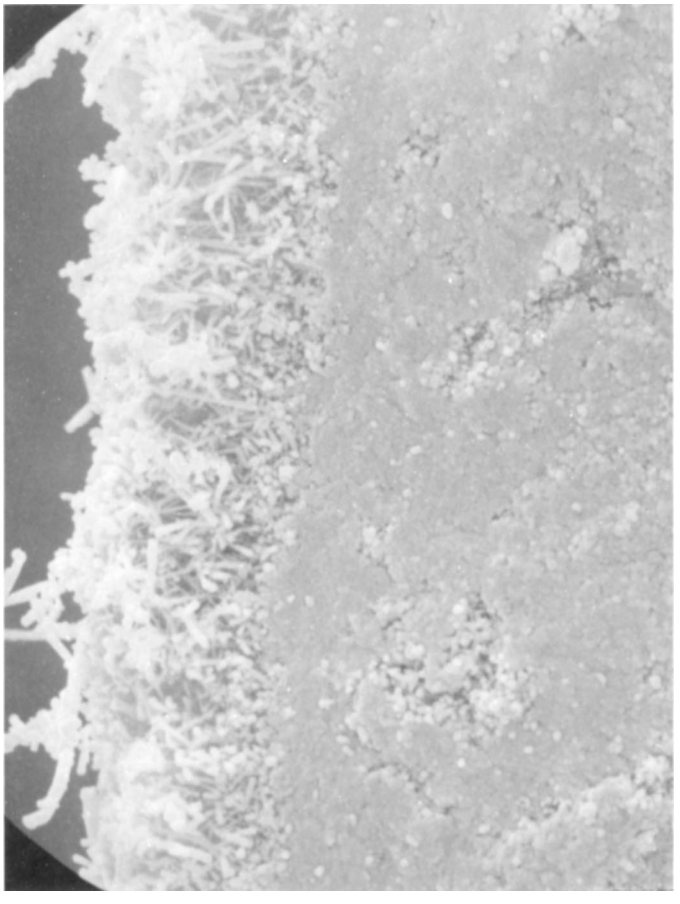

FIG. 9. 10 μm. SiC whisker growth at the surface and substantial densification owing to methane addition.

The nitrogen isotherm at 77 K has been used to evaluate the texture and thus the potential of this support in catalysis. The BET method and the *t*-method then give the total surface area, the meso-/macro-pore surface area, and the micro-pore volume. The results are shown in Table 3. A distinction is made between the converted carbon prior to and after removal of the residual carbon. Pretreatment in hydrogen of a nickel loaded activated carbon results in a small increase in surface area (BET and *t*) and micro-pore volume owing to the gasification, which takes place during the pretreatment. The surface area after conversion has been reduced from 981 m^2/g to values between 395 and 154 m^2/g (after oxidation; i.e., removal of residual carbon the surface area ranges from 57 to 32 m^2/g); the pore volume decreases from 0.67 ml/g to a value between 0.18 and 0.27 ml/g (after oxidation: 0.37–0.15 ml/g). These changes can predominately be ascribed to a decrease in micro-pore surface area and pore volume, showing that the micro-pore structure is blocked during conversion.

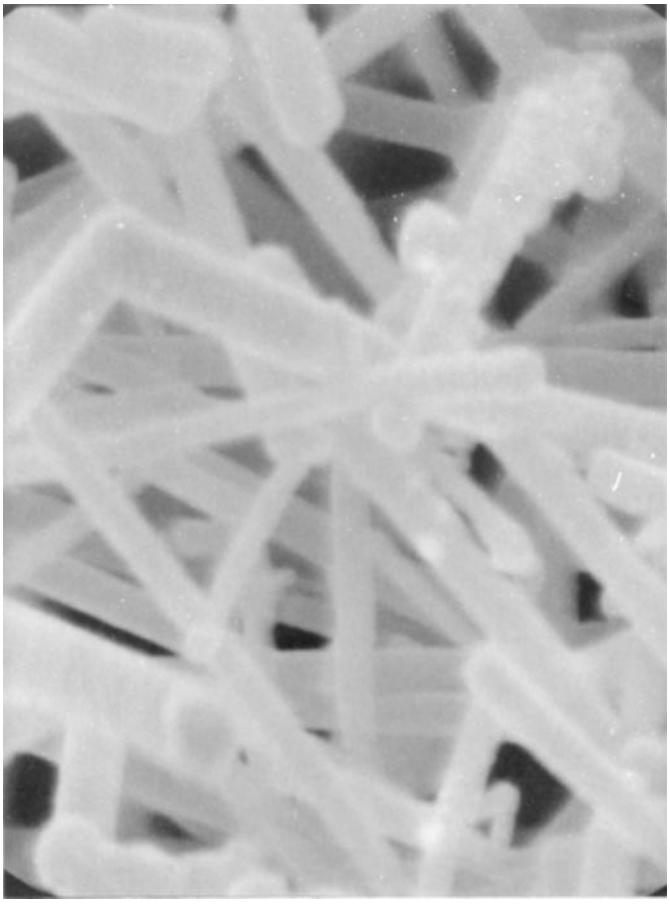

FIG. 10. 1 μm. Whiskers at the exterior of an extrudate as a result of added methane.

4. DISCUSSION

Several characteristics of the catalyzed carbon conversion emerge from the results described above. First of all, the optimal temperature when utilizing nickel as catalyzing species is established by XRD to be around 1380 K. Moreover, higher nickel contents seem to improve the conversion properties of the system. To gain full insight in the occurring mechanism, however, elaboration of these observations regarding the chemical aspects and mass-transfer considerations of the process are indispensable.

TABLE 3

Texture of SiC Supports Synthesized by Carbon Conversion at 1380 K and 8 kPa

Material		S_{BET} (m^2/g)	V_{pore} (cm^3/g)	S_t (m^2/g)	V_{micro} (cm^3/g)
RW08		947	0.60	112	0.41
2 wt% Ni/RW08	Pretreated	981	0.67	115	0.44
2 wt% Ni/RW08[a]	Converted	395	0.22	215	0.10
	Oxidized	57	0.37	57	0
5 wt% Ni/RW08[a]	Converted	154	0.21	58	0.027
	Oxidized	32	0.21	31	0
8 wt% Ni/RW08[a]	Converted	189	0.18	88	0.041
	Oxidized	36	0.15	33	0
5 wt% Ni/RW08[b]	Converted	270	0.27	77	0.091
	Oxidized	48	0.29	43	0

[a] $H_2/SiCl_4 = 26$, reaction 3600 s.
[b] $H_2/SiCl_4 = 16$, reaction 3000 s.

4.1. Chemical Aspects

SEM analysis of extrudates containing 2 wt% Ni which are converted at 1075 K displays the presence of small SiC granules of 0.3 μm diameter. The amount of deposited material and morphology of this system is comparable to that of modified activated carbon by methyl trichlorosilane and nickel catalysis at 1073 K. This is confirmed by the deposition of SiC on the quartz-wool pads outside the extrudates. These observations suggest that the carbon species which is active in the formation of SiC, utilizing $SiCl_4$ as silicon precursor, has been supplied *via* the gas phase. Formation of gaseous carbon species can be achieved according to the well-known hydrogasification of solid carbon as shown in Table 4. SiC deposition then ensues *via* the second reaction. Silicon formation will be encountered as a consequence of the reduction of $SiCl_4$ by hydrogen. The values of the enthalpy, entropy, and free Gibbs energy of reactions 1, 2, and 3, calculated from the Janaf thermochemical tables (18) are shown in Table 4 for the optimal SiC formation conditions, i.e. 1400 K and 10 kPa.

4.1.1. Hydrogasification of carbon. Hydrogasification at 1400 K and 10 kPa is thermodynamically not favoured as shown by the positive ΔG. The maximum equilibrium amount of methane formed under reaction conditions is 0.4 mol%. This explains that hydrogasification at these conditions is feasible, although not favoured by thermodynamics. In general, two classes of hydrogasification catalyzed by group VIII metals can be distinguished.

The first one, typically encountered at temperatures below 800 K, consists of dissociative adsorption of hydrogen on the metal surface and subsequent spillover of H atoms to the graphite zones where methane production takes place (19). The second class involves dissolution of carbon at the Ni–C interface, diffusion of carbon in Ni, and reaction of carbon with chemisorbed hydrogen at the Ni–gas interphase (20, 21). This mechanism develops at temperatures

TABLE 4

ΔH, ΔS, and ΔG for the Reactions during SiC Synthesis at 1400 K and 10 kPa

	Reaction	ΔH (kJ/mol)	ΔS (J/(mol K))	ΔG (kJ/mol)
1	$C + 2H_2 \rightleftarrows CH_4$	−92.31	−136.8	99.18
2	$SiCl_4 + CH_4 \rightleftarrows SiC + 4HCl$	297.1	298.9	−121.4
3	$SiCl_4 + 2H_2 \rightleftarrows Si + 4HCl$	277.6	169.6	40.08

above 800 K and is probably operative in the described conversion of activated carbon.

4.1.2. Silicon carbide formation. XRD analysis has shown that conversion at 1250 K results in an considerable amount of SiC formed. The angle between the platelets present at the surface of the extrudate (70°) corresponds very well with values reported by Knippenberg for twinning in β- and α-SiC (70°33′) (22). These dendritic crystals originate from secondary nucleation of SiC on long whiskers at the outer part of the extrudate as shown by Fig. 3. These branches form a skeleton which is filled up by continuous deposition between the platelets as displayed in Fig. 4. The thickness of these platelets (0.1 μm) corresponds well to that of the whiskers. Consecutive growth finally results in bamboo-like structures as shown by Fig. 5, which in turn can be branched as well. The outlined mechanism is in agreement with the SiC growth phenomena described by Knippenberg (22). At the interior of the extrudates SiC-granules (0.3 μm diameter) are formed as well.

Carbon conversion at 1378 K results in the formation of large amounts of SiC as is shown by the X-ray diffractograms in Fig. 2. The substantial increase primarily originates from the catalyzed SiC whisker growth by the vapour–liquid–solid (VLS) mechanism. Excessive whisker growth is visible throughout the entire extrudate. Figure 6 is an example of a whisker explosion, which has probably been nucleated by a large nickel crystallite. The VLS mechanism has been introduced by Wagner and Ellis in 1964 (23) and has successfully been applied in whisker syntheses. Prior to their report the model proposed by Sears (24) assumed that whisker growth was initiated by a screw dislocation at the top of the growing crystal. Molecules that adsorbed at the whisker surface either diffused to the top of the whisker and would be incorporated in the crystal round the screw axis or desorb. This model left, however, much unclarified. Furthermore, only a few materials, like palladium, exhibited a screw dislocation at the top of the whisker (25). The research of Wagner and Ellis was focused on the growth of silicon whiskers by the reduction of $SiCl_4$ by hydrogen at 1323 K and the influence of certain impurities thereof. They reported that (1) silicon whiskers do not contain an axial screw dislocation at the top of the Si-whisker, (2) the presence of certain impurities are indispensable for whisker growth, and (3) a liquid-like globule is present at the tip of the whisker during growth. The impurity (in their case gold) forms under reaction conditions a liquid droplet which acts as a preferred site for adsorption of the gaseous Si-precursor. The surface of this droplet can be considered as atomically rough; this situation is similar to that of a (111) surface on which every surface site resembles an attractive growth site, which is attended by a high accommodation coefficient or sticking coefficient. Besides the adsorption process at the V-L surface (and concomitant chemical reactions), two other processes are of importance in the VLS mechanism, i.e. diffusion through the liquid droplet and incorporation of atoms in the crystal at the L-S interface. In principle, each of these processes can be the rate limiting step, but in most cases the incorporation of atoms in the crystal is considered to be rate limiting.

Growth of SiC whiskers can be catalyzed by several metals. Bootsma *et al.* (26) reported the use of iron in the system $SiO_2/C/H_2$ at 1473 to 1573 K. Heating to 1473 K resulted in the formation of Fe–Si–C droplets. The droplet diameters vary in the same range as the initially applied Fe particles (1 to 40 μm). These Fe–Si–C droplets are formed by taking a small amount of the substrate into solution, forming a shallow etch pit. After saturation with SiC, the etch pit is refilled by SiC growth and the alloy is lifted upwards. This process is typical for situations in which the substrate consists of one of the constituents of the whisker. Motojima and Hasegawa (27) grew β-SiC whiskers utilizing a gas mixture containing Si_2Cl_6, CH_4, H_2, and Ar. Several metallic components (group VIIIa of the periodic system according to IUPAC) have been investigated for their catalytic effect on whisker growth. The following sequence was established in which the catalytic effect ranges from strongly positive to negative; $Co > Ni > Cu \approx Cr \approx Au > Mn$. Especially cobalt and nickel were shown to be very effective catalysts. The velocity of whisker formation is found to be in the order of several millimetres per hour, which is common for whisker growth, but high for conventional CVD processes. The minimal temperature for Co catalyzed whisker growth from Si_2Cl_6 is reported to be 1300 K. Nickel catalyzed growth with $SiCl_4$ as Si precursor is shown to be the best combination in the parameter area investigated. SiC whiskers were formed above 1363 K, whereas the use of cobalt necessitates temperature above 1443 K. The observations regarding the nickel catalyzed whisker growth are in agreement with the results attained in the conversion of activated carbon into SiC; substantial SiC formation is found at 1378 K.

4.1.3. Silicon codeposition. The X-ray diffractograms sometimes display the presence of crystalline silicon. The point at which this codeposition starts shifts to longer durations of conversion for higher nickel loadings (e.g., 3600 s for 2 wt% Ni and 7200 s for 5 wt% Ni). Silicon codeposition can be attributed to deactivation of the nickel catalyst which takes part in the catalytic hydrogasification of the carbon. Reaction with the ash of the carbon, contamination of nickel by dissolution of some silicon, or encapsulation by deposited SiC, are most likely the causes of deactivation. Thus, the concentration of gaseous carbon species in the extrudate diminishes, resulting in Si codeposition. Chin *et al.* (28) decomposed CH_3SiCl_3 (MTS) to form SiC and report that the transitions between the zones of stoichiometric SiC deposition and silicon codeposition encountered on the substrate were not sharp but showed a gradual change in Si : C ratio in the deposits as the process parameters varied.

X-ray diffraction displayed the presence of large amounts of Si, while electron probe micro analysis revealed an average composition of $Si_{1.18}C$. The excess silicon is incorporated in the SiC structure as small crystals as shown by Minatu *et al.* (29). Free silicon is seen as small white spots in optical micrographs, which decrease in size and number at higher deposition temperatures. Silicon is reported to be invisible by SEM analysis. The addition of methane (30) or propane (31) to CH_3SiCl_3 generally results in less extensive Si formation. Stoichiometric SiC is then deposited at 1600 K (for CH_4) and 1473 K (for C_3H_8) using C/Si ratios of 2. A C/Si ratio of 3.4 is necessary at 1473 K to deposit SiC from a CH_4/CH_3SiCl_3 mixture. These reported observations are valid for H/Si ratio greater than 100. The use of lower H/Si ratios is expected to lower the necessary temperature or C/Si reactant ratio (5) in order to achieve stoichiometric SiC. The reason for silicon deposition during carbon conversion is thus to be conceived as methane deficiency during SiC deposition, imposed by the deactivation of gasifying nickel. The extent of deactivation increases with increasing conversion time, the C/Si ratio drops simultaneously, which causes at a certain moment the formation of free Si during SiC growth. The maximum achievable carbon conversion depends on the initial amount of gasifying nickel and the deactivation rate thereof and will be discussed in Section 4.2.

The addition of methane during carbon conversion results in minor Si-deposition as shown by XRD (Fig. 8), extensive densification, and the formation of a more extensive micrograined SiC structure. The Si codeposition can be rationalized by the fact that the relative extent of noncatalyzed SiC formation increases, which apparently requires a higher C to Si ratio in the gas phase (30, 31) than that in the case of catalytic SiC formation. It can thus be concluded that silicon is codeposited during SiC growth with a deficiency of gaseous carbon species, rather than an abrupt shift from SiC to Si deposition at the end of the conversion procedure.

The next section deals with the evaluation of the possible presence of mass-transfer limitations during the conversion of activated carbon into SiC.

4.2. Mass Transport Phenomena

Kinetic measurements in catalytic studies are often disguised by mass-transport limitations of the reactants or products. Very fast surface reactions result thus in severe concentration gradients inside the catalyst pellet. These gradients in turn can impose the formation of external diffusion limitations. Both types of mass-transfer limitations are well known in the field of catalysis and chemical vapour deposition. Obvious instances of internal mass-transport limitations can be found in the field of chemical vapour infiltration (32). Chemical vapour deposition on flat surfaces can suffer from mass-transport limitations as well. Concentration gradients present in the diffusion layer around the surface can determine to a large extent the morphology of the deposits. Diffusion limited growth will result in deposits containing voids and a rough surface morphology owing to the enhancement of surface fluctuations during deposition. Kinetically controlled processes, however, will cause the formation of smooth surfaces. With the aid of thermal gravimetric analysis (TGA) the reaction rate of CH_4 and SiC formation has been determined. These figures are used to investigate the possible existence of diffusional limitations in this system of carbon conversion. Figure 11 shows the overall rates of CH_4 and SiC formation for carbon conversions of 3600 s utilizing 2, 5, and 8 wt% Ni on carbon. The values given in Fig. 11 are average rates of the entire conversion period. Similar rates of formation of CH_4 and SiC are found for the carbon containing 2 wt% Ni. Both reaction rates increase with increasing amounts of nickel. The formation of methane is, however, enhanced to a larger extent. This process will cause higher carbon conversions but incomplete conversions of methane into silicon carbide as shown by Fig. 12. The observations described above seem to disagree with the thermodynamic calculations (Table 4). The subsequent reaction of methane with silicon tetrachloride to form silicon carbide is expected to consume the total amount of methane present in the pores of the extrudates. This effect can either have a kinetic or mass-transfer origin. The first is not likely to occur, because it would implicate that, when the total nickel content is increased, the amount of nickel responsible for the gasification increases to a larger extent than the amount of nickel which catalyzes the VLS growth of SiC. Mass-transport limitations, however, are to be expected in the experiments described above, owing to the high reaction rates encountered when the VLS mechanism is operative.

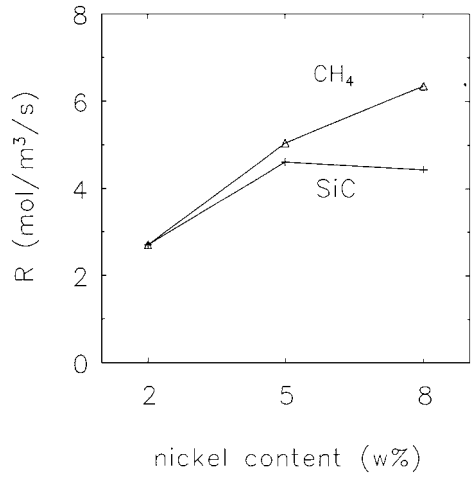

FIG. 11. Reaction rates for SiC and CH_4 formation as a function of nickel content, 3600 s reaction.

Internal diffusion limitations are easily evaluated utilizing the Wheeler–Weizs number, which is the product of the effectiveness factor and the square of the Thiele modulus. This number can be calculated using observable quantities

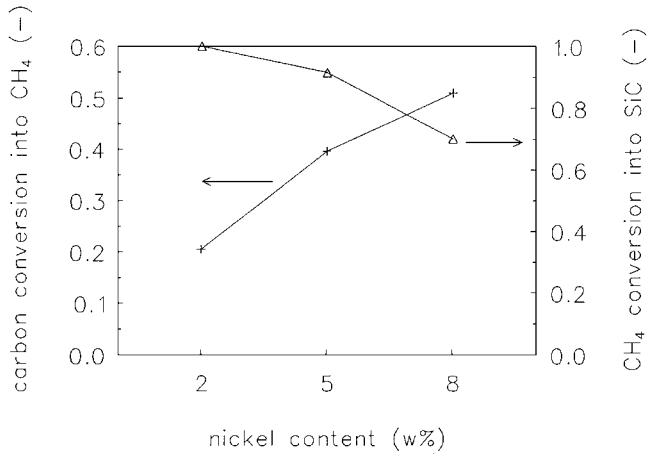

FIG. 12. CH_4 selectivity (+) and carbon conversion (△) as a function of the nickel content.

according to Eq. [1] (32).

$$\eta\varphi^2 = R_{obs}L^2/D_{eff}C_b, \qquad [1]$$

where η is the effectiveness factor, φ is the Thiele modulus, R_{obs} is the observed reaction rate in mol/s, L is a characteristic diffusion length (V_{pore}/A_{pore}), D_{eff} is the effective diffusion coefficient, and C_b represents the concentration of the diffusing species in the gas phase. The effectiveness factor is close to one in the absence of internal mass-transfer limitations which results in the criterion for those conditions,

$$\eta\varphi^2 < 0.15. \qquad [2]$$

The effective diffusion coefficient is determined concordant the procedures given in (33). External concentration gradients can be observed in the presence of internal diffusion limitations. The Carberry number (Ca) is convenient for the evaluation of the magnitude of these gradients. It represents the relative concentration difference over the film around the particle and is calculated according to Eq. [3],

$$\mathrm{Ca} = R_{obs}/k_g a' C_b, \qquad [3]$$

where k_g is the mass-transfer coefficient and a' is the specific area per unit volume (A_p/V_p). A relative concentration difference of 5% over the film (i.e., $\mathrm{Ca} < 0.05$) is assumed to be the criterion from which external diffusion limitations are significant. For low Reynolds numbers ($5 < \mathrm{Re} < 500$) the mass transfer coefficient can be determined from the following correlation in which the Stanton (St) and Schmidt (Sc) numbers are used (34).

$$\mathrm{St}\cdot\mathrm{Sc}^{2/3} = (0.81 \pm 0.05)\mathrm{Re}^{-0.5} \qquad [4]$$

with

$$\mathrm{St} = \frac{k_g\epsilon_b}{U_f}, \quad \mathrm{Re} = \frac{\rho_f U_f d_p}{\eta_f}, \quad \mathrm{Sc} = \frac{\eta_f}{\rho_f D_g}, \qquad [5], [6], [7]$$

where ρ_f denotes the density of the gas, ϵ_b is the porosity of the bed, U_f is the superficial gas velocity, d_p is the particle diameter, and η_f represents the viscosity of the gas.

The following conditions (Table 5) are used as an example in the determination of mass transfer limitations. The density and viscosity of hydrogen are assumed to be representative for the total gas mixture which consists of at least 80 mol% H_2. Silicon tetrachloride has been assumed to represent the major abundant gaseous Si species. The reaction rates of methane and silicon carbide formation in the conversion of 2 wt% Ni/C have been used to evaluate the possible presence of internal and external diffusion limitations.

Internal mass-transfer limitations are evaluated depending on the pore dimensions of the carbon. In general, a trimodal pore distribution is encountered in activated carbon which imposes the necessity of considering micro-, meso-, and macro-pores independently for the estimation of internal diffusion limitations. The results of applying the values of Table 5 for the calculation of the transport properties are displayed in Table 6. Calculation of the effective diffusion coefficients reveals that internal mass transport is in all cases primarily determined by the Knudsen regime, resulting in a tenfold higher overall diffusion coefficient for hydrogen compared to that of $SiCl_4$. Internal mass-transfer limitations are present for the $SiCl_4$ species invariably of the pores considered. It should be noted that thermodynamic calculations have shown that at these conditions the amount of $SiCl_2$ approaches the amount of $SiCl_4$ (5). The diffusion coefficient of $SiCl_2$ is only 30% larger (Knudsen regime) than that of $SiCl_4$, which also results in large internal mass-transfer limitations. Diffusion limitations for hydrogen are encountered in the micro-pores as well as the meso-pores. The Carberry numbers are in all cases smaller

TABLE 5

Numerical Values Applied in the Calculations

Reactor			
Temperature	T	1378	K
Pressure	P	10	kPa
Bed length	L_b	0.8×10^{-3}	m
Bed porosity	ϵ_b	0.4	m^3 gas/m^3 reactor
Bed diameter	d_b	0.04	m
Support properties			
Mean radius micro pore	r_{mi}	0.6	nm
Mean radius meso pore	r_{me}	10	nm
Mean radius macro pore	r_{ma}	400	nm
Tortuosity	τ	4	m^2 gas/m^2 particle
Porosity	ϵ_p	0.7	m^3 gas/m^3 particle
Input gas (at reactor conditions)			
Flow	ϕ_f	2.21×10^{-6}	kg/s
Space velocity	U_f	1.04	m/s
Density	ρ_f	1.7×10^{-3}	kg/m^3
Viscosity	η_f	2.4×10^{-5}	Pa s
Specific heat	C_p	15.93	J/(kg K)

TABLE 6

Mass Transfer Characteristics for H_2 and $SiCl_4$ in the Conversion of Extrudates Containing 2 wt% Ni

	Diffusion coefficients (10^{-6} m^2/s)			Dimensionless numbers	
	$SiCl_4$	H_2		$SiCl_4$	H_2
$D_{eff,\,mi}$	0.03	0.27	Re	0.05	0.05
$D_{eff,\,me}$	0.48	4.4	Sc	2.6	0.97
$D_{eff,\,ma}$	19	170	St	1.9	3.7
	Wheeler–Weizs			Carberry	
	$SiCl_4$	H_2		$SiCl_4$	H_2
$\eta\varphi^2_{mi}$	1106	9.4	k_g	5	10
$\eta\varphi^2_{me}$	66	0.60	Ca	<0.05	<0.05
$\eta\varphi^2_{ma}$	1.7	0.01			

than 0.05, which means that external concentration gradients can be neglected for both the hydrogen as well for the silicon tetrachloride. The extent of internal mass-transfer limitations is calculated for the 5 and 8 wt% Ni/C systems as well; silicon tetrachloride suffers in all these cases from severe transport limitations. The Wheeler–Weizs moduli of hydrogen are depicted in Fig. 13.

Internal diffusion limitations of hydrogen increase using higher nickel loadings. These limitations, however, are absent in the macro-pores of the carbon. The observed levelling off of the rate of formation of silicon carbide while the rate of methane formation enhances at increasing nickel loadings is thus shown to originate from mass-transfer limitations of silicon tetrachloride.

Figure 14 presents the mechanism which envisages the mass transfer considerations as well as the chemical aspects on an atomic scale. Hydrogen is present throughout the carbon extrudate; its concentration decreases to some extent, moving to the middle of the extrudate. The presence

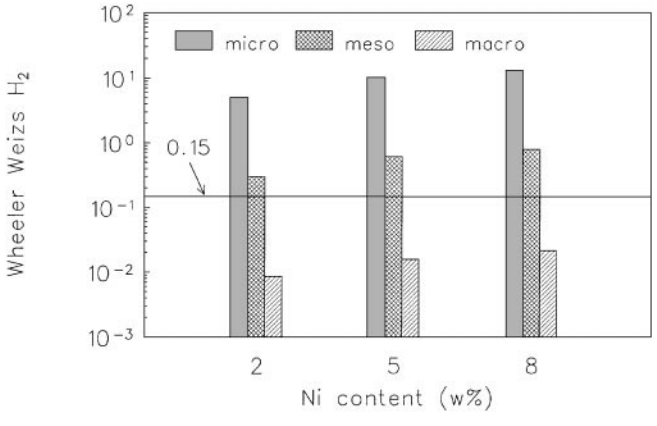

FIG. 13. Wheeler–Weizs number of H_2 in the micro-, meso-, and macro-pores for various nickel loadings (1 h reaction).

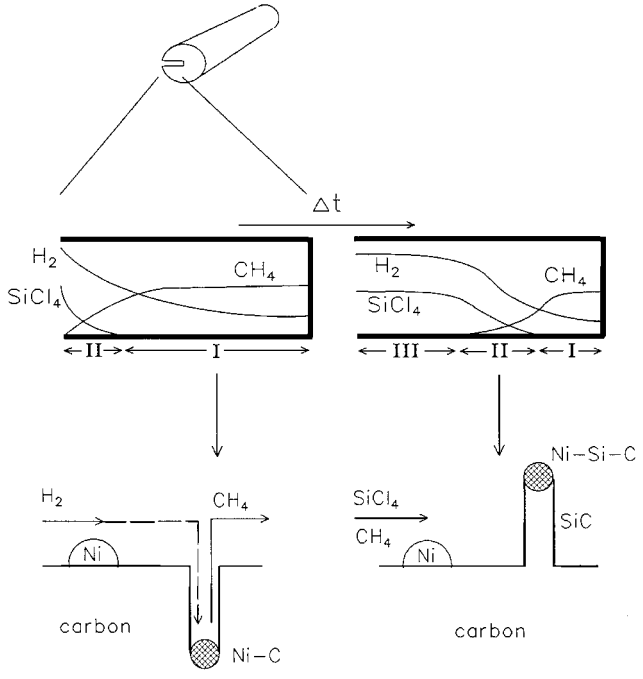

FIG. 14. The mechanism of nickel catalyzed conversion of activated carbon extrudates by reactive chemical vapour deposition, region I: hydrogasification; II: hydrogasification and whisker growth; III: possible Si deposition.

of silicon tetrachloride, however, is in the initial stage of conversion mainly limited to the outer layer of the porous structure. Hydrogasification and whisker growth occur simultaneously in the presence of $SiCl_4$ (region II). Region I is encountered inside the extrudate, where hydrogen is the only reactant present. In this initial period excess methane is formed at the interior of the extrudate which accounts for the incomplete CH_4 conversion into SiC as shown by Figs. 11 and 12 for the 5 and 8 wt% Ni/C extrudates. The amount of $SiCl_4$ diffusing into the porous structure does not suffice for the total methane conversion. The carbon conversion process after this period is to be conceived as a moving front of silicon carbide formation going from the outside to the inside, while methane is being formed throughout the particle. The extent of penetration of region II in the pore in the initial stage is determined by the rate of CH_4 formation and the rate of $SiCl_4$ diffusion.

The position of the front is stationary if these rates are identical. The inwards movement of the SiC formation front starts when the inward flow of $SiCl_4$ exceeds the outward flow of CH_4. This is induced by the deactivation of gasification sites, resulting in a decrease in the rate of gasification. The deactivation is most probably caused by the reaction of nickel with the ash present in the carbon. Additionally, the silicon tetrachloride is to be expected to increase this rate of deactivation of the gasification sites by forming a Ni–Si alloy (probably Ni_3Si) when moving inwards. Hence, a third zone (region III) is induced where both $SiCl_4$ and

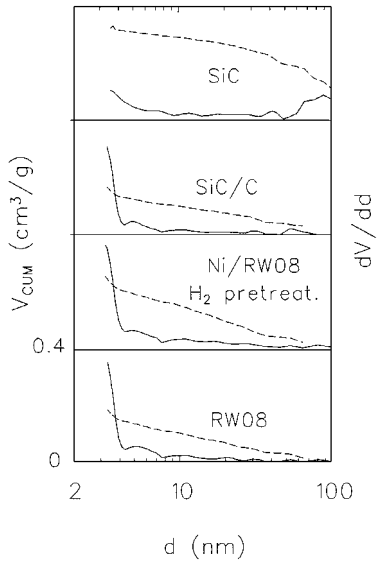

FIG. 15. Cumulative (– – –) and differential (———) pore volume distribution of the RW08, H_2 pretreated (Ni/RW08), converted (SiC/C), and the converted activated carbon after removal of carbon (SiC).

H_2 are present in large amounts, whereas CH_4 is nearly absent. Silicon codeposition can then occur in region III via Si codeposition during SiC growth.

4.3. Catalyst Properties

The textural properties of a catalyst support determine to a large extent the feasibility of application. Utilization of silicon carbide is, however, *a priori* limited to those fields in which substantial advantages are obtained over application of conventional catalyst supports (SiO_2, Al_2O_3, and activated carbon), due to the foreseen higher production costs. In general SiC formation is a highly endothermic process causing high energy processing costs. Additionally the SiC formation is a high-temperature reaction, which requires high capital costs for the reactor. Areas in which silicon carbide may be employed are (1) high-temperature reactions, (2) liquid-phase reactions at demanding pH conditions, and (3) reactions in which the inertness of the silicon carbide surface is crucial. The exact manner of application depends on the achieved surface area and pore distribution. The surface areas of all synthesized SiC supports lay in the high surface area range (above 20 m^2/g) which is, compared to that of α-Al_2O_3, sufficient for high-temperature applications. Catalytic operations at high temperatures, e.g. steam reforming of methane (35), suffer generally from severe diffusional limitations. Moreover, mass transport in catalyst pellets at high temperature (above 1000 K) mainly occurs in the Knudsen regime, which implicates that the pore radius determines to a large extent the rate of diffusion. Hence, wide pore catalyst supports are most suitable, where moderate surface areas (i.e., $\approx$20 m^2/g) at normal pore volumina suffice. The remaining nickel is generally present as nickel silicide, which is not known to be a catalytically active material. When metallic nickel or nickel oxides are, however, present, these can be easily removed by an acid washing procedure.

Elaboration of the nitrogen isotherms results in Fig. 15, which displays the cumulative and differential pore volume distributions, calculated using the corrected Kelvin equation, for all four stages in the synthesis. Note that only the meso/macro part of the pore size distribution is given.

An increase at diameters below 4 nm is appearing, indicating the onset of the micro-pore region for original, H_2 pretreated, and the converted carbon. The major part of the pore volume of the silicon carbide support, however, is positioned in the meso/macro-pore region which means that the entire surface area is available for catalysis. Additionally, the meso/macro-pore volume of the high surface area SiC is larger than the original carbon. The absence of micro-pore volume is shown as well by the equal values of S_{BET} and S_t (Table 3). Figures 16 and 17 are micrographs of the SiC support which shows that this type of conversion enables the synthesis of wide-pore SiC extrudates. The homogeneous conversion is confirmed in Fig. 16, while Fig. 17

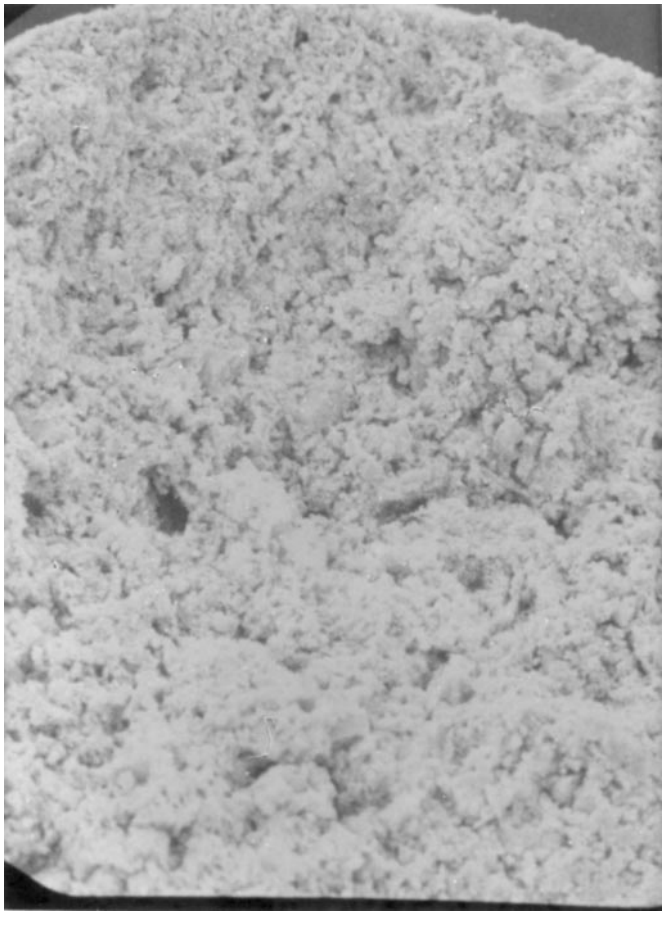

FIG. 16. 100 μm. Micrograph of the SiC support which shows the preservation of the extrudate shape.

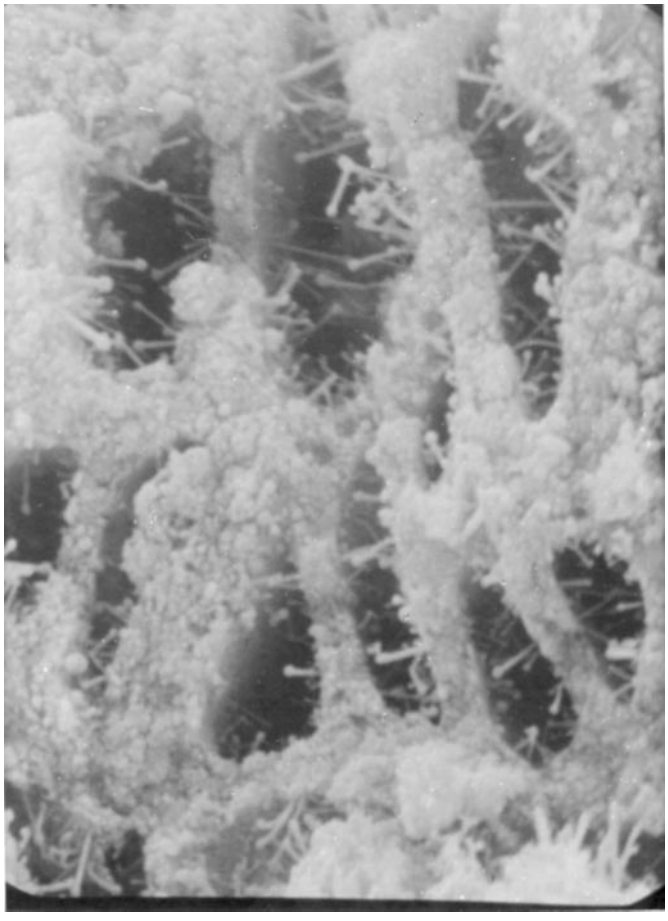

FIG. 17. 5 μm. Magnification of Fig. 16, which shows the morphology of high surface area SiC.

displays the two types of SiC formation. Conventional SiC deposition results in the formation of granules, which act as support of the whiskers grown by the VLS mechanism.

5. CONCLUSIONS

A novel method has been developed for the synthesis of high surface area silicon carbide. It comprises the reaction of nickel loaded activated carbon extrudates with silicon tetrachloride and hydrogen at 1380 K and 10 kPa to form silicon arbide. Reaction at temperatures below 1380 K results in silicon codeposition. A dual catalytic action of nickel has been observed, *viz*. hydrogasification: $C(s) + 2H_2(g) \rightleftarrows CH_4(g)$ and SiC formation $SiCl_4(g) + CH_4(g) \rightleftarrows SiC(s) + 4HCl(g)$. The total carbon conversion depends on the amount of nickel used and ranges from 20 to 55% for 2 and 8 wt% Ni, respectively. The operative vapour–liquid–solid mechanism causes the abundance of SiC whiskers throughout the converted extrudates. Calculation of mass-transport numbers shows that in the initial stage of conversion methane is formed in the entire extrudate, whereas SiC formation is limited to the outer part. This is the consequence of severe internal diffusion limitations of $SiCl_4$. Deactivation of gasification sites causes the inwards movement of SiC formation, until all gasification sites are deactivated and the conversion is ended. The surface areas of the SiC/C composites range from 154 to 395 m^2/g. Oxidation of the residual carbon at 1023 K results in high surface area SiC (57 m^2/g to 32 m^2/g). The meso/macro porous texture allows utilization of this catalyst support (1) at high temperature and (2) in liquid-phase reactions.

SYMBOLS

a'	specific area per unit volume (m^2/m^3)
A_p	external surface area of particle (m^2)
A_{pore}	specific surface area (m^2/g)
C_b	the concentration of the diffusing species in the gas phase (mol/m^3)
C_p	specific heat (J/kg/K)
d_p	particle diameter (m)
D_g	gas-phase diffusion coefficient (m^2/s)
D_{eff}	effective diffusion coefficient (m^2/s)
$D_{Knudsen}$	Knudsen diffusion coefficient (m^2/s)
k_g	Mass-transfer coefficient (m/s)
L	characteristic diffusion length (m)
L_b	length of bed (m)
M_w	mol weight (g/mol)
$r_{mi,me,ma}$	radius of micro, meso, or macro pore (m)
R	reaction rate (mol/m^3_{carbon}/s)
R_{obs}	the observed reaction rate (mol/s)
T	temperature (K)
U_f	superficial gas velocity (m^3 gas/(m^2 reactor s))
V_p	volume particle (m^3)
V_{pore}	pore volume (m^3/g)
w_0	weight after pretreatment (kg)
w_{ash}	amount ash of pretreated carbon (kg)
$w_{gasif.}$	weight loss due to gasification (kg)
w_t	weight after conversion (kg)
$w_{SiC/Si/C}$	amount SiC/Si/C after conversion (kg)

Greek

ϵ_b	porosity of the bed (m^3 gas/m^3 reactor)
ϵ_p	porosity of the particle (m^2 gas/m^2 particle)
η	effectiveness factor (−)
η_f	viscosity of the gas (Pa s)
ϕ_f	mass flow (kg/s)
φ	Thiele modulus (−)
ρ_f	density of the gas (kg/m^3)
τ	tortuosity (−)

Dimensionless Numbers

Ca	Carberry
Re	Reynolds
Sc	Schmidt
St	Stanton

ACKNOWLEDGMENT

This research was part of of the Innovation-oriented Research Programme on Catalysis (IOP, Project number 90017) and was financially supported by the Ministry of Economic Affairs of The Netherlands.

REFERENCES

1. Duchet, J. C., van Oers, E. M., de Beer, V. H. J., and Prins, R., *J. Catal.* **80**, 386 (1983).
2. Stegenga, S., "Automotive Exhaust Catalysis without Noble Metals," thesis, University of Amsterdam, The Netherlands, 1991.
3. Jungten, H., *Fuel* **65**, 1436 (1986).
4. Stegenga, S., van Waveren, M., Kapteijn, F., and Moulijn, J. A., *Carbon* **30**, 577 (1992).
5. Moene, R., Boon, H. Th., Makkee, M., and Moulijn, J. A., *Carbon* **34**, 567 (1996).
6. Moene, R., Makkee, M., Schoonman, J., and Moulijn, J. A., "Carbon '92, Proceedings of the 5th Carbon Conference, Essen, German Carbon Group, 1992," p. 474.
7. Levy, R. B., *in* "Advanced Materials in Catalysis" (J. J. Burton and R. L. Garton, Eds.), p. 101. Academic Press, New York, 1977.
8. Leclerq, L., *in* "Surface Properties and Catalysis by Non-metals" (J. P. Bonnelle, B. Delmon, and E. G. Derouane, Eds.), p. 433. Reidel, Dordrecht, 1983.
9. Oyama, S. T., *Catal. Today* **15**, 179 (1992).
10. Chorley, R. W., and Lednor, P. W., *Adv. Mater.* **3**, 474 (1991).
11. Pham-Huu, C., Del Galls, P., Peschieva, E., and Ledoux, M. J., *Appl. Catal. A* **132**, 77 (1995).
12. Ledoux, M. J., Hantzer, S., Pham-Huu, C., Guille, J., and Desaneaux, M.-P., *J. Catal.* **114**, 176 (1988).
13. Vincent, H., Ponthenier, J. L., Porte, L., Vincent, C., and Bioux, J., *J. Less-Commen Met.* **157**, 1 (1990).
14. Reid, R. C., Prausnitz, J. M., and Poling, B. E., "The Properties of Gases and Liquids," 4th ed., p. 632. McGraw-Hill, New York, 1993.
15. Boublik, T., Fried, V., and Hala, E., "The Vapour Pressures of Pure Substances," p. 32. Elsevier Scientific, Amsterdam, 1973.
16. Brunauer, S., Emmett, P. H., and Teller, E., *J. Amer. Chem. Soc.* **60**, 309 (1938).
17. de Boer, J. H., Linsen, B. G., and Osinga, Th. J., *J. Catal.* **4**, 643 (1965).
18. Janaf Thermochemical Tables, 3rd ed., *J. Phys. Chem. Ref. Data*, Vol. 14, 1985.
19. Orlander, D. R., and Balooch, M., *J. Catal.* **60**, 41 (1979).
20. Goethel, P. J., and Yang, R. T., *J. Catal.* **108**, 356 (1987).
21. Tsamopoulos, J. A., Dandekar, H. W., and Scholtz, J. H., *J. Catal.* **117**, 549 (1989).
22. Knippenberg, W. F., "Growth Phenomena in Silicon Carbide," thesis, RU Leiden, The Netherlands, 1963.
23. Wagner, R. S., and Ellis, W. C., *Appl. Phys. Lett.* **4**, 89 (1964).
24. Sears, G. W., *Acta Met.* **1**, 457 (1953). [**3**, 361 (1955).]
25. Givargizov, E. I., *in* "Current Topics in Materials Science" (E. Kaldis, Ed.), Vol. 1, p. 79. North Holland, Amsterdam, 1978.
26. Bootsma, G. A., Knippenberg, W. F., and Verspui, G., *J. Crystal Growth* **11**, 297 (1971).
27. Motojima, S., and Hasegawa, *J. Crystal Growth* **87**, 311 (1988).
28. Chin, J., Gantzel, P. K., and Hudson, R. G., *Thin Solid Films* **40**, 57 (1977).
29. Minato, K., and Fukuda, K., *J. Mater. Sci.* **23**, 699 (1988).
30. Kuo, D. H., Cheng, D. J., Shyy, W. J., and Hon, M. H., *J. Electrochem. Soc.* **137**, 3688 (1990).
31. Choi, B. J., Jeun, S. H., and Kim, D. R., *J. Europ. Ceram. Soc.* **9**, 357 (1992).
32. Moulijn, J. A., Tarfaoui, A., and Kapteijn, F., *Catal. Today* **11**, 1 (1991).
33. Moene, R., Dekker, J. P., Makkee, M., Schoonman, J., and Moulijn, J. A., *J. Electrochem. Soc.* **141**, 282 (1994).
34. Perry, R. H., and Green, D. W., "Perry's Chemical Engineer's Handbook," 6th ed., pp. 4–45. McGraw–Hill, New York, 1984.
35. Rostrup–Nielsen, J. R., "Steam Reforming Catalysts," p. 34. Danish Technical Press Inc., Copenhagen, 1973.